







# Very High Resolution SAR Imaging With DGPS-Supported Airborne X-Band Data

Yashi Zhou , Pei Wang , Zhen Chen , Qingchao Zhao , Wei Wang , Lei Zhang, Weidong Yu, *Member, IEEE*, Yunkai Deng, *Member, IEEE*, and Robert Wang , *Senior Member, IEEE*

**Abstract**—High spatial resolution imaging in synthetic-aperture radar (SAR) can provide accurate monitoring capacity and has been gaining great attention recently in the fields of military and civilian. Apparently, the slant range resolution of the SAR system depends on the radar operating bandwidth. Currently, the large bandwidth signal synthesizing technology of the stepped frequency chirp signal waveform is highly practical for achieving high spatial resolution. However, the system structure and the corresponding signal processing technology become more complex. In order to verify the feasibility and operability of the large full-bandwidth system, a 3.6-GHz full-bandwidth airborne experimental SAR system operating at X-band, featured by full-bandwidth transmitting and receiving, has been designed by the Department of Space Microwave Remote Sensing System, Institute of Electronics, Chinese Academy of Sciences, as a test bed for the development and implementation of the future spaceborne realizations. For this large full-bandwidth SAR system, in addition to the hardware resource, the motion compensation (MOCO) is an urgent problem. The improvement of spatial resolution will aggravate the effect of motion errors. In order to focus the SAR images accurately, this article presents a technical approach by utilizing the differential global positioning system (DGPS) technology to improve the position accuracy of the inertial measurement unit device. Meanwhile, considering the significant deviation of range cell migration correction (RCMC) due to the residual range-variant errors, this article proposes an accurate MOCO strategy with DGPS-supported to implement the second-order MOCO, space-variant residual range envelope, and space-variant residual phase error in azimuth before RCMC. Finally, this article presents the outfield experiment and reports the corresponding analysis and processing results of an outfield flight experiment successfully conducted in March 2019.

**Index Terms**—3.6 GHz full-bandwidth, high spatial resolution imaging, synthetic-aperture radar (SAR).

## I. INTRODUCTION

SYNTHETIC-APERTURE radar (SAR), featured by acquiring radar images at any time day or night and under

Manuscript received April 14, 2020; revised June 4, 2020; accepted June 16, 2020. Date of publication June 22, 2020; date of current version July 3, 2020. This work was supported in part by the National Key Research and Development Program under Grant 2017YFB0502700, in part by the National Science Fund for Distinguished Young Scholars under Grant 61825106, and in part by the National Science Fund under Grant 61701479. (*Corresponding author: Pei Wang.*)

Yashi Zhou, Zhen Chen, and Qingchao Zhao are with the University of Chinese Academy of Science, Beijing 100190, China. (e-mail: zhouyashi16@mails.ucas.ac.cn; chenchen171@mails.ucas.ac.cn; zqc\_nudt@163.com).

Pei Wang, Wei Wang, Lei Zhang, Weidong Yu, Yunkai Deng, and Robert Wang are with the Department of Space Microwave Remote Sensing System, Institute of Electronics, Chinese Academy of Science, Beijing 100190, China (e-mail: vanpei@163.com; ww\_nudt@sina.com; 314forever@163.com; ywd@mail.ie.ac.cn; ykdeng@mail.ie.ac.cn; yuwang@mail.ie.ac.cn).

Digital Object Identifier 10.1109/JSTARS.2020.3004013

all-weather conditions, is a crucial sensor for earth observation. Meanwhile, it becomes the focus of research on remote sensing technology and also has been playing an important role in applications of Earth's environment in the last decades [1]–[6]. High spatial resolution is an important emerging requirement for Earth dynamic monitoring, e.g., vegetation mapping, soil moisture determination, mineral exploration, urban mapping, and maritime domain surveillance. The higher the spatial resolution, the more information will be obtained [7]. However, the slant range resolution of SAR system depends on the radar operating bandwidth. Therefore, in order to improve the resolution ability of ground scatterers, the radar operating bandwidth is the core.

In recent years, the large bandwidth signal synthesizing technology of the stepped frequency chirp signal waveform is well documented for achieving high range resolution [8]–[10]. An obvious advantage of the stepped-frequency technology mentioned above is the reduction of the instantaneous system bandwidth and the corresponding sampling rate requirements of the SAR system [11]. Therefore, several systems have utilized larger bandwidth synthesizing technology, such as 760 MHz with the F-SAR [12], 1.2 GHz with the ROOFSAR [13], 1.8 GHz with the phased array multifunctional imaging radar (PAMIR) [14], 3.6 GHz with the upgraded PAMIR [15], and 4 GHz with the RAMSES-NG [16]. In terms of the hardware resources, although the stepped-frequency technology mentioned above can overcome the issues of the A/D device, system clock, and the active electronically steered array antenna, the corresponding system structure and the signal processing technology of the large bandwidth signal synthesizing will become more complex. Meanwhile, it also brings many new problems between the receiving channels, such as the amplitude/phase/delay imbalances, slant errors, spectrum leakage, etc., which will affect the bandwidth signal synthesizing and directly determine the quality of high spatial resolution imaging. Therefore, the large full-bandwidth transmitting and receiving system and the corresponding signal processing technology are a more meaningful research work.

However, the large full-bandwidth system for achieving high-resolution imaging also faces many challenges. In addition to the hardware resource (i.e., the realization of transceiver link limited by the bottleneck of A/D and D/A conversion rate), the signal processing is also an urgent problem, particularly for the motion compensation (MOCO) techniques. Motion errors, resulting from the trajectory deviations, will induce range delay and azimuth phase errors (APEs) that can severely degrade the SAR image quality [17]. The reason is that in terms of the large



Fig. 1. Employed airborne platform.

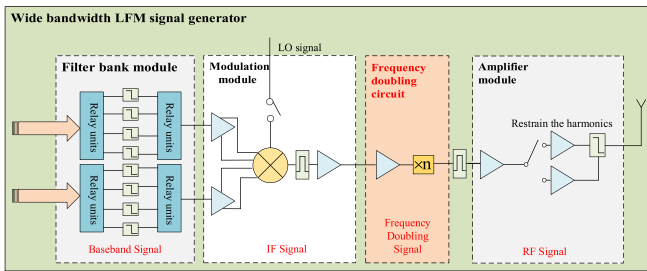


Fig. 2. Block diagram of wide-bandwidth LFM signal generator.

full-bandwidth SAR system (i.e., the ultra-high-resolution SAR system), the improvement of spatial resolution will aggravate the effect of motion errors [18]. That is to say, there will exist a residual migration in several or even dozens of range cells and significant high-order APEs [19]. Therefore, the high-accuracy inertial navigation systems/global positioning systems (GPS) and an accuracy MOCO strategy should be utilized to correct motion errors.

From the perspective of the technological development, airborne SAR systems have always been a step ahead in terms of technical development, allowing the demonstration of new techniques and applications that were later implemented in spaceborne SAR missions [20]. During the airborne experiment, the practical engineering problems may possess potential value for the implementation of the future spaceborne realizations. In order to verify the feasibility and operability of the large full-bandwidth system, a 3.6-GHz full-bandwidth airborne experimental SAR system operating at X-band, featured by full-bandwidth transmitting and receiving, has been designed by the Department of Space Microwave Remote Sensing System, Institute of Electronics, Chinese Academy of Sciences, and an outfield experiment was successfully conducted in March 2019, as shown in Fig. 1, where the SAR antenna mounted at the bottom of the airborne is marked in red.

To generate the wide-bandwidth LFM signal of 3.6 GHz, this system utilizes the orthogonal modulation and the frequency doubling technology to avoid the bottleneck of the D/A conversion rate. The frequency doubling circuit structure is shown in Fig. 2. First of all, this wide-bandwidth modulation source mentioned above modulates the baseband video signal and local oscillator signal to IF signal. After that, pass-through frequency

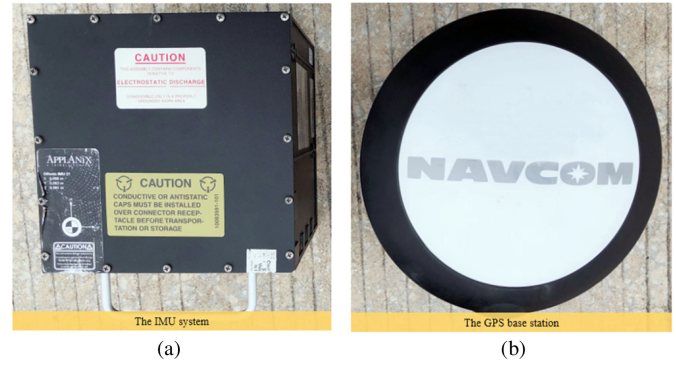


Fig. 3. Practical POS. (a) IMU system. (b) Ground-mounted GPS base station.

doubling, amplifying and filtering, and the radar target radio frequency signal with the bandwidth of 3.6 GHz can be obtained. On receiving, the data recorder samples the full-bandwidth LFM signal and receives the auxiliary data from the master computer.

The rest of this article is organized as follows. In Section II, the measuring principle of the positioning and orientation system (POS) with differential GPS (DGPS) technology is described. The signal model and the acquisition geometry of an airborne platform are shown in Section III. For the MOCO, the related analytical work and the corresponding correction method are presented in Section IV. The processing procedure of high-resolution imaging is shown in Section V. The simulation results are shown in Section VI. The experiment results and the conclusion are shown in, Sections VII and VIII, respectively.

## II. MEASURING PRINCIPLE OF THE POS SYSTEM WITH DGPS

POS, also known as an inertial measurement unit (IMU) with GPS, is a high-accuracy motion measurement equipment. A version of the POS AV610 was utilized in this experiment. The IMU system was mounted over the antenna. An additional GPS base station was placed on the ground. The output of the IMU system is adjusted according to the high precise DGPS postprocessing data in real time, which can be acquired from the ground-mounted GPS base station and the airborne-mounted GPS facility with differential technique. The POS system precisely measures aerial sensor position and orientation hundreds of times each second (i.e., the sampling frequency is 200 Hz). The accuracy of the position and velocity can reach 0.03 m and 0.005 m/s, respectively. The practical system is shown in Fig. 3.

### A. Coordinate Transform of the POS System

For the device of the airborne platform, once placed, the accurate geometric relationships can be determined among the airborne-mounted GPS facility (mounted at the top of platform), IMU, and the SAR antenna (mounted at the bottom of platform). The geometric relationship of POS-integrated sensors is shown in Fig. 4. First, a coordinate system is established with the geometric center of the SAR antenna as the origin, and the X-axis denotes the flight direction. Then, the eccentricities of the antenna center relative to IMU and the airborne-mounted

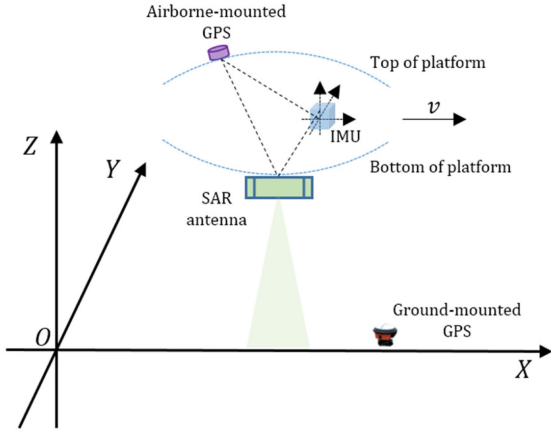


Fig. 4. Geometric relationship of POS-integrated sensors.

GPS facility can be calculated by accurate measurement. Finally, according to the relative relationship of the eccentricities mentioned above and the corresponding coordinate transform, the spatial position and orientation information of the SAR antenna center can be calculated based on GPS data and IMU observation data and further fit the nominal trajectory.

### B. DGPS Postprocessing

GPS measurements are affected by various errors, such as ionosphere, troposphere, satellite clock, receiver clock offset, receiver noise, and multipath [21]. Generally speaking, the ionosphere, troposphere, and clock offset errors have good spatial correlation. In other words, due to the measurement of the same satellites, when two observation stations at shorter distance conduct single-point orientation experiment, the above-mentioned errors remain almost constant over a small-sale area. That is to say, when the position of one GPS base station through surveying is accurately known, these common errors can be estimated and subtracted. For the accurately known GPS station, the actual range can be obtained from the satellite ephemeris data. Then, the corresponding pseudorange of the known ground-mounted GPS station can be described as [22]

$$\rho_G = r_G + C(\delta t_G - \delta t_S) + I_{\rho_G} + T_{\rho_G} + \varepsilon_{\rho_G} \quad (1)$$

$$e_G = \rho_G - r_G \quad (2)$$

where  $r_G$  is the actual range of the ground-mounted GPS station. And  $\delta t_G$  and  $\delta t_S$  represent the GPS station and satellite clock biases, respectively. And  $I_{\rho_G}$  and  $T_{\rho_G}$  represent the corresponding delay of the ionosphere and troposphere, respectively.  $\varepsilon_{\rho_G}$  denotes the noise and measurement errors. In conclusion,  $e_G$  is the constant errors mentioned above.

Considering the constant errors over a small-sale area, for the measurement of the airborne-mounted GPS, the actual position can be corrected as

$$\rho_{A'} = \rho_A - e_G \quad (3)$$

where  $\rho_A$  denotes the pseudorange of the airborne-mounted GPS. Therefore, the position accuracy can be improved after correction of the constant errors mentioned above.

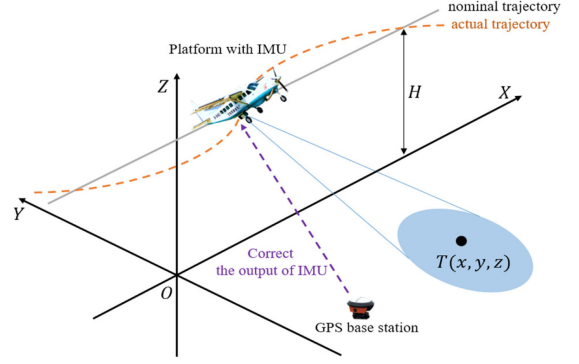


Fig. 5. Imaging geometry of the side-looking strip-map mode with POS.

In our field experiment, an additional and accurately known position ground-mounted GPS base station and the airborne-mounted GPS facility conduct GPS observation within 30 km at the same time. Therefore, these errors can be computed [23] and further correct the position results of the IMU system output, which contributes to the subsequent MOCO work.

### III. SIGNAL MODEL AND DATA ACQUISITION GEOMETRY

The data acquisition geometry of an airborne platform with the POS system is shown in Fig. 5. The solid straight line parallel to the X-axis and the dashed curve denote the nominal trajectory and the actual trajectory, respectively. The height of the nominal trajectory is  $H$ . For the nominal trajectory, the antenna phase center (APC) of the radar moves along the X-axis at a constant velocity of  $V$ . Therefore, the actual and nominal APC positions are  $[V \cdot t + \Delta x(t), \Delta y(t), H + \Delta z(t)]$  and  $[V \cdot t, 0, H]$  at a slow time  $t$ , respectively. And  $\Delta x(t)$ ,  $\Delta y(t)$ , and  $\Delta z(t)$  denote the motion displacements between the nominal and the actual trajectory. For an arbitrary target  $T(x, y, z)$  in the scene, the closet range of this target in the nominal trajectory can be denoted as  $r_T = \sqrt{(H - z)^2 + y^2}$ . Then, the instantaneous slant range at a slow time  $t$  between this target and the nominal trajectory is  $R_0(t, r_T) = \sqrt{r_T^2 + (V \cdot t - x)^2}$ . Taking the motion displacement into account, the practical instantaneous slant range  $R(t)$  between this target and the actual trajectory can be written as [24]

$$R(t) = \sqrt{(V \cdot t + \Delta x(t) - x)^2 + (\Delta y(t) - y)^2 + (H + \Delta z(t) - z)^2} \\ = R_0(t, r_T) + \Delta R(t, r_T) \quad (4)$$

$$\Delta R(t, r_T) = \Delta R_c(t, r_c) + \Delta R_v(t, r_T) \quad (5)$$

where  $\Delta R(t, r_T)$  denotes the range displacement in the line-of-sight (LOS) direction, and  $r_c$  is the shortest slant range of the scene center.  $\Delta R_c(t, r_c)$  and  $\Delta R_v(t, r_T)$  represent the displacement errors corresponding to the range-invariant at the scene center and the residual range-variant at the target  $T(x, y, z)$ , respectively.

Ignoring the impact of the envelope and applying fast Fourier transform in the range direction, the echo spectrum of the target



TABLE I  
MAIN PARAMETERS OF THE AIRBORNE SAR SYSTEM

Parameter	Value
Carrier frequency	9.6 GHz
Velocity	80 m/s
Signal pulse duration	15 us
PRF	3000 Hz
Signal bandwidth	3600 MHz
Height	3600 m
Incidence angle	60 deg

$T$  can be expressed as

$$S_r(t, f_r, r_T) = \exp\left\{-j\pi\frac{f_r^2}{K_r}\right\} \cdot \exp\left\{-j\frac{4\pi}{c}(f_r + f_c)\right. \\ \left.[R_0(t, r_T) + \Delta R_c(t, r_c) + \Delta R_v(t, r_T)]\right\} \quad (6)$$

where  $K_r$  is the chirp rate,  $f_c$  is the central frequency of the transmitted linear frequency-modulated signal, and  $f_r$  is the range frequency.

#### IV. RELATED ANALYTICAL WORKS AND CORRECTION METHOD

This 3.6-GHz full-bandwidth SAR system was mounted on a midsize fixed-wing aircraft (see Fig. 1), which flew over 3600 m above the ground with a mean velocity of approximately 80 m/s. In this experiment, the SAR antenna operated with the off-nadir-angle of  $60^\circ$  (in the right-looking geometry) and emitted pulse waveform with the azimuth antenna size of 0.496 m. Therefore, the synthetic-aperture length in azimuth and the swath width in range are approximately 400 m and 1.25 km, respectively. The approximate theoretical spatial resolutions of the azimuth and ground range are 0.28 m and 0.046 m, respectively. Meanwhile, the corresponding spatial sampling interval of the azimuth  $d_a$  and the slant range  $d_r$  is 0.0267 m and 0.0341 m, respectively. The main configuration parameters of this airborne SAR system are summarized in Table I.

Due to the ultra-high-resolution of this SAR system, the effect of motion errors will be aggravated for high-quality images. Therefore, an accurate MOCO strategy is crucial for the ultra-high-resolution airborne SAR processing. In this experiment, the attitude variations have been eliminated by serving the real antenna so that the center of the antenna beam points a fixed look direction. Therefore, in the following analysis, the motion errors are divided into two parts, i.e., the forward velocity error and the displacement error in LOS direction. As shown in Fig. 6, the motion displacements between the nominal and the actual trajectory are local zoomed.  $\Delta x$  denotes the displacement caused by the forward velocity error at a slow time  $t$ .  $\Delta y$  and  $\Delta z$  denote the corresponding displacement errors in the LOS direction.

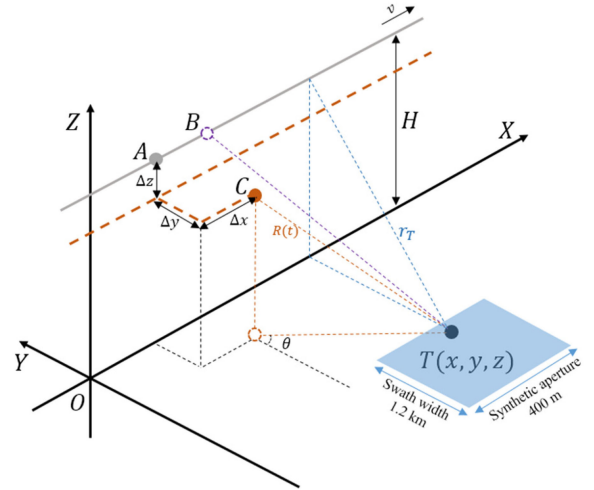


Fig. 6. Local zooming of the motion displacements.

#### A. Correction of the Displacement Error in the LOS Direction

1) *Phase Error Compensation*: Generally speaking, the range displacements in the LOS direction can be divided into the range-invariant part at the scene center and the residual range-variant part, respectively. A simple method can be implemented under the range-invariant assumption [25]. Unfortunately, the range-invariant assumption mentioned above is not satisfactory for the ultra-high-resolution SAR system. In [26], the reasonability of two-steps MOCO method has been systematically deduced. It assumes that the range-variant part has no effect on the subsequent range cell migration correction (RCMC). A representative two-steps MOCO approach has been proposed, taking the range invariant (i.e., the first-order MOCO) and the residual range-variant (i.e., the second-order MOCO) components [27] into account. The former is corrected with respect to the scene center before RCMC, and the latter is performed after the range cell migration (RCM) compensation finished. Unfortunately, for this 3.6-GHz full-bandwidth ultra-high-resolution SAR system, the range sampling interval is of the order of centimeters. Therefore, even small residual range-variant components will result in significant effect on RCMC and further result in the azimuth defocus, particularly for the boundary targets.

Meanwhile, due to the range-variant errors in LOS, the range variance of envelope errors can be ignored through dividing the range compressed data into subswath. But, it is worth noting that the precise range envelope of each range cell is not compensated, particularly at the boundary of a subswath.

Therefore, there will exist a phase mismatch of the phase compensation between the actual trajectory and the nominal trajectory, particularly for this 3.6-GHz SAR system. For the ultra-high-resolution SAR system, the image quality is sensitive to the accuracy phase. In [28], the phase mismatch induced by the approximate range envelope compensation is analyzed. Therefore, in order to reduce the effect on phase mismatch, the phase compensation should be implemented before the range envelope [28]. In practical, the record data of POS system correspond to

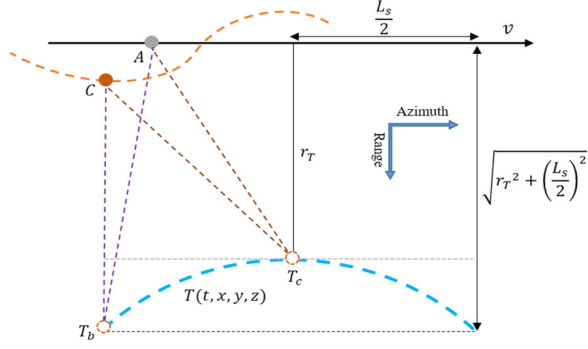


Fig. 7. Second-order MOCO before RCMC.

the actual trajectory, which distinguishes from the slant range relative to the nominal trajectory of the conventional one-step MOCO algorithm. Therefore, the actual range displacement of LOS should express as follows:

$$r_{s,n} = r_0 + n \cdot \frac{c}{2f_s}, \quad n = 0, 1, 2, \dots, N_r - 1 \quad (7)$$

$$r_{s,n_g} = \sqrt{r_{s,n}^2 - (H - \Delta z(t))^2} \quad (8)$$

$$\Delta R(t, n) = r_{s,n} - \sqrt{(r_{s,n_g} \cdot \cos \theta + \Delta y(t))^2 + (r_{s,n_g} \cdot \sin \theta)^2 + H^2} \quad (9)$$

where  $r_0$  is the actual slant range of the first range bin, and  $r_{s,n}$  corresponds to the slant range between target and actual trajectories.  $f_s$  denotes the range sampling frequency.  $r_{s,n_g}$  represents the corresponding actual ground range.  $\theta$  is the squint angle of antenna beam.

Based on the analysis mentioned above, in order to reduce the effect on RCMC, in this article, we implement the second-order MOCO for each range cell by combining with the first-order MOCO before RCM compensation. Meanwhile, the standard Omega-K algorithm is more ideal for the ultra-high-resolution imaging without approximation and can well combine with the second-order MOCO before implementing the step of Stolt interpolation. The corresponding mathematical expressions are shown in the following.

After the range compression and the first-order MOCO, the echo signal in time domain can be written as

$$s_r(t, t_r, r_T) = \text{sinc} \left\{ \Omega_r \left( t_r - \frac{2R_0(t, r_T)}{c} \right) \right\} \cdot \exp \left\{ -j \frac{4\pi}{\lambda} [R_0(t, r_T) + \Delta R_v(t, r_T)] \right\} \quad (10)$$

where  $\Omega_r$  and  $t_r$  represent the range bandwidth and range time, respectively.

Then, the compensation of the residual range-variant components can be implemented for each range cell based on (10). It is worth noticing that there will exist residual phase error, which is induced by the range-variant compensation due to the curved RCM line  $T(t, x, y, z)$ . As shown in Fig. 7, it is assumed that the target  $T_c$  locates at the boundary of the range swath and the

corresponding slant of the RCM line is expressed as  $R(t, r_T)$  in blue color. When we implement the second-order MOCO, the range-variant component of target  $T_b$  should be compensated according to the point of  $T_b$  rather than  $T_c$ . Therefore, the maximum residual phase error  $\Delta\varphi_{\max}$  introduced by the RCM can be represented as follows:

$$\Delta\varphi_{\max}(t, r_T) = \exp \left\{ -j \frac{4\pi}{\lambda} [\Delta R_v(t, r_T) - \Delta R_{v,\max}(t, R_b(t, r_T))] \right\} \quad (11)$$

where

$$R_b(t, r_T) =$$

$$\sqrt{\left( V \cdot t + \Delta x(t) - x + \frac{L_s}{2} \right)^2 + (\Delta y(t) - y)^2 + (H + \Delta z(t) - z)^2} \quad (12)$$

$$R_{b0}(t, r_T) = \sqrt{r_T^2 + \left( V \cdot t - x + \frac{L_s}{2} \right)^2}. \quad (13)$$

Then, the maximum range-variant components of target  $T_b$  can be expressed as

$$\Delta R_{v,\max}(t, R_b(t, r_T)) = R_b(t, r_T) - R_{b0}(t, r_T) - \Delta R_c(t, r_c) \quad (14)$$

where  $L_s$  and  $T_a$  denote the practical synthetic-aperture length and the corresponding synthetic-aperture time, respectively. And  $R_{b0}(t, r_T)$  represents the slant range corresponding to the boundary point of a synthetic length (i.e., the point of  $T_b$  in Fig. 7) at a slow time  $t$ .

Based on the analysis mentioned above, the maximum residual phase error depends on the RCM. As a general evaluation criterion of  $\pi/4$ , the residual phase error can be ignored when the maximum value is less than this evaluation criterion. For the ultra-high-resolution SAR system, the effect of residual phase error mentioned above on image quality is more obvious. Actually, as long as the range envelope can be corrected within a proper single range cell, the residual APE mentioned above can also be compensated by utilizing the frequency division algorithm [29] before RCMC. The azimuth spectrum is divided into several blocks, and each block is processed with angle-variable narrow beam MOCO.

2) *Space-Variant Range Envelope Compensation*: For the space-variant range envelope compensation, the conventional literatures do not take the space-variant characteristic into account, or the space-variant range envelope is approximately equal to the range-invariant envelope of the subswath center. To a certain extent, although the space-variant range envelope can be neglected by dividing the compressed data into subswaths, the noncentral targets of the subswath area would arise the twisted, symmetrical and raised sidelobe (see Section VI), which has serious implications for the subsequent space-variant residual phase error compensation and the azimuth focus quality. Especially, for the 3.6-GHz ultra-high-resolution SAR system, the phenomenon mentioned above is more obvious due to the

high-range sampling frequency. Therefore, the space-variant range envelope compensation would be implemented by range resampling according to the actual range displacement interval  $\Delta R(t, n)/d_r$  of the LOS direction.

### B. Correction of the Forward Velocity Error

Forward velocity variations can result in additional image quality degradation [30]. Some cases, such as low resolution and extremely steady airborne platform, can ignore the effect of forward velocity. However, for the ultra-high-resolution and small airborne platform, the most immediate effects are the nonuniform spatial sampling interval due to the variant forward velocity. As shown in Fig. 6, after the correction of the displacement error in the LOS direction, the position of platform has been corrected from the point  $C$  (located at the actual trajectory) to the point  $B$  (located at the nominal trajectory). Then, the displacement along the nominal trajectory exists only the interval of  $\Delta x$ . Due to the oversampling with high PRF, the spectral aliasing effect is ignorable in the azimuth direction. Therefore, as shown in Fig. 9, an azimuth resampling method is utilized for processing the effect of the forward velocity variation after the correction of the displacement in the LOS finished. In this case, the conventional two-steps MOCO method is inappropriate for combining with the azimuth resampling.

### C. Space-Variant Residual Phase Error Compensation

For the ultra-high-resolution SAR system, the space-variant residual phase error compensation would be affected by the range-variant displacement error if implemented after RCMC. After space-variant residual RCM envelope compensation and azimuth resampling, the actual trajectory has been corrected to the nominal trajectory (i.e., point  $C$  turns into point  $A$  in Fig. 7). Then, the residual phase error can be corrected as follows:

$$\Delta\varphi_T(t, x, y, z) = \exp \left\{ j \frac{4\pi}{\lambda} [|AT_c| - |AT(t, x, y, z)|] \right\}. \quad (15)$$

Utilizing the frequency division algorithm to improve the processing efficiency, we can obtain the azimuth squint angle  $\beta_k$  of the  $k$ th azimuth subaperture

$$\beta_k = \sin^{-1} \left( \frac{\lambda f_{a,k}}{2V} \right). \quad (16)$$

Then, the shift value  $\Delta a_k$  of the center in the  $k$ th azimuth subaperture can be expressed as

$$\Delta a_k(t) = \sqrt{(r_{n,g} \cdot \cos \theta - \Delta y(t))^2 + (r_{n,g} \cdot \sin \theta)^2 + (H + \Delta z(t))^2} \cdot \tan \beta_k \quad (17)$$

$$r_{n,g} = \sqrt{\left( r_0 + n \cdot \frac{c}{2f_s} \right)^2 - H^2}. \quad (18)$$

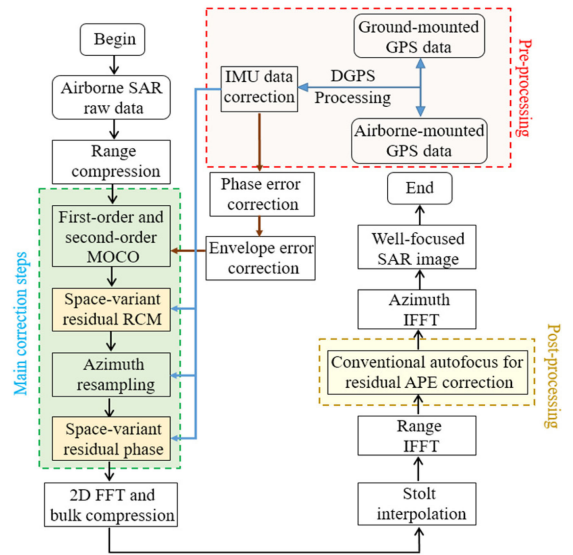


Fig. 8. Main flowchart of the processing procedure.

Then, the ideal slant range of the center in the  $k$ th azimuth subaperture can be expressed as (19), where  $r_{n,g}$  denotes the slant range of the  $n$ th range cell (19) shown at the bottom of the page.

Then, the space-variant residual phase error can be corrected

$$\tilde{s}(t, n) = \sum_k s_k(t, n) \cdot \exp \left\{ j \frac{4\pi}{\lambda} \left( \left( r_0 + n \cdot \frac{c}{2f_s} \right) - r_{n,k,\text{real}}(t) \right) \right\} \quad (20)$$

where  $s_k(t, n)$  denotes the corresponding time-domain echo signal of the  $k$ th azimuth spectrum after the residual range envelope compensation and azimuth resampling.

## V. PROCESSING PROCEDURES

As mentioned in Section III, the outputs of the IMU system is adjusted according to the high precise DGPS postprocessing data in real time; however, the sampling frequency of POS system is only 200 Hz, which is below the sampling frequency PRF of the data record of the SAR system. Therefore, the output of POS system was implemented the interpolation processing to keep steps to the data record of the SAR system. For the ultra-high-resolution SAR imaging, considering the significant effect on RCMC due to the residual range-variant components, the second-order MOCO is implemented before the step of Stolt interpolation. Based on the analysis mentioned above, the main flowchart of the processing procedure is shown in Fig. 8. It consists of the preprocessing steps, main MOCO correction steps, and the postprocessing steps.

$$r_{n,k,\text{real}}(t) = \sqrt{\left( \sqrt{(r_{n,g} \cdot \cos \theta - \Delta y(t))^2 + (r_{n,g} \cdot \sin \theta)^2} - \Delta a_k(t) + \Delta y(t) \right)^2 + (\Delta a_k(t))^2 + H^2} \quad (19)$$



Fig. 9. Azimuth resampling diagram.

 TABLE II  
 MAIN PARAMETERS OF THE SIMULATION EXPERIMENT

Parameter	Value
Carrier frequency	9.6 GHz
Velocity	80 m/s
Signal pulse duration	5 us
PRF	1800 Hz
Signal bandwidth	1200 MHz
Height	3600 m
Incidence angle	60 deg

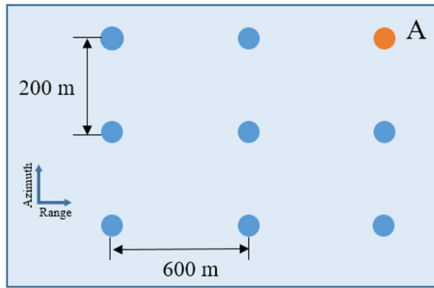


Fig. 10. Distribution of the simulation points.

## VI. SIMULATION RESULTS OF THE CORRECTION METHOD

As aforementioned, for the ultra-high-resolution SAR system, the improvement of spatial resolution will aggravate the effect of motion errors. Therefore, an accurate MOCO method should be applied to reduce the effect of motion errors. Here, a simulation experiment was carried out to confirm the effectiveness of the MOCO correction method mentioned above for the ultra-high-resolution imaging. To be more descriptive, high-frequency motion errors were added into the simulation experiment as follows. In a real scenario, the motion errors are far greater than the additional errors. The detailed system parameters are shown in Table II. The distribution of the simulation targets is coincident with the real scene, as shown in Fig. 10

$$\Delta x(t) = 5 \cdot d_r \cdot \sin\left(\frac{2\pi}{T_a} \cdot 3 \cdot t\right) \quad (21)$$

$$\Delta y(t) = 5 \cdot d_a \cdot \sin\left(\frac{2\pi}{T_a} \cdot 3 \cdot t + \frac{\pi}{8}\right) \quad (22)$$

$$\Delta z(t) = 5 \cdot d_r \cdot \sin\left(\frac{2\pi}{T_a} \cdot 3 \cdot t + \frac{\pi}{4}\right) \quad (23)$$

where  $d_r$  and  $d_a$  denote the sampling intervals in range and azimuth directions, respectively.  $T_a$  corresponds to the synthetic-aperture time. Meanwhile, the different initial phase errors are

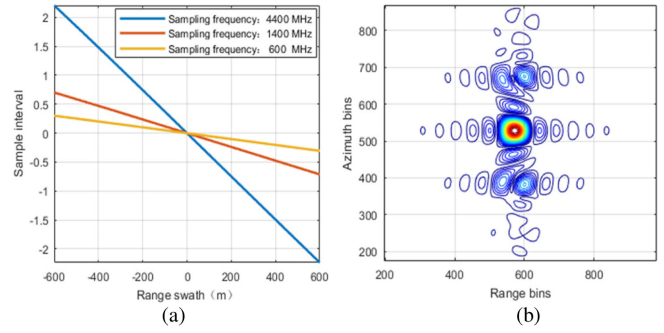


Fig. 11. Effect of the space-variant range envelope. (a) Space-variant range displacement interval varying with sampling frequency. (b) Corresponding contour plot of the target A.

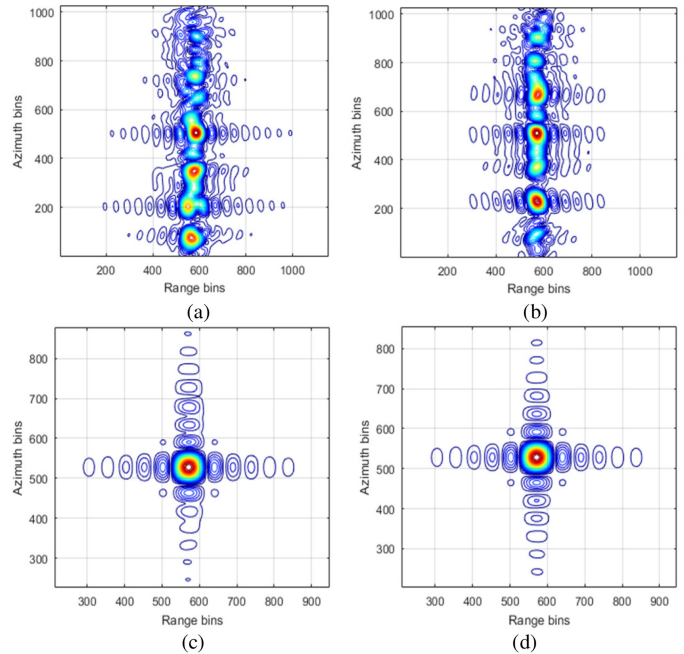


Fig. 12. Simulation results of the proposed processing procedure. (a) After first-order and second-order MOCO. (b) After space-variant residual range envelope compensation. (c) After azimuth resampling. (d) After space-variant residual phase compensation.

added into simulation experiment. The space-variant range displacement interval varying with sampling frequency is shown in Fig. 11.

In order to analyze the effect of the space-variant range envelope, the error  $\Delta x$  was set to zero. As shown in Fig. 11, the space-variant range displacement interval varies with the range sampling frequency. The higher the sampling frequency is, the greater the space-variant range displacement interval is. Although the residual range envelope is much less than one sampling interval, the corresponding contour plot of the target A arises the twisted, symmetrical, and raised sidelobe when the space-variant range envelope is neglected by dividing the compressed data into subswath. It has serious implications for the subsequent space-variant residual phase error compensation and the azimuth focus quality, particularly at the ultra-high sampling frequency (e.g. 4.4 GHz). Based on the analysis mentioned



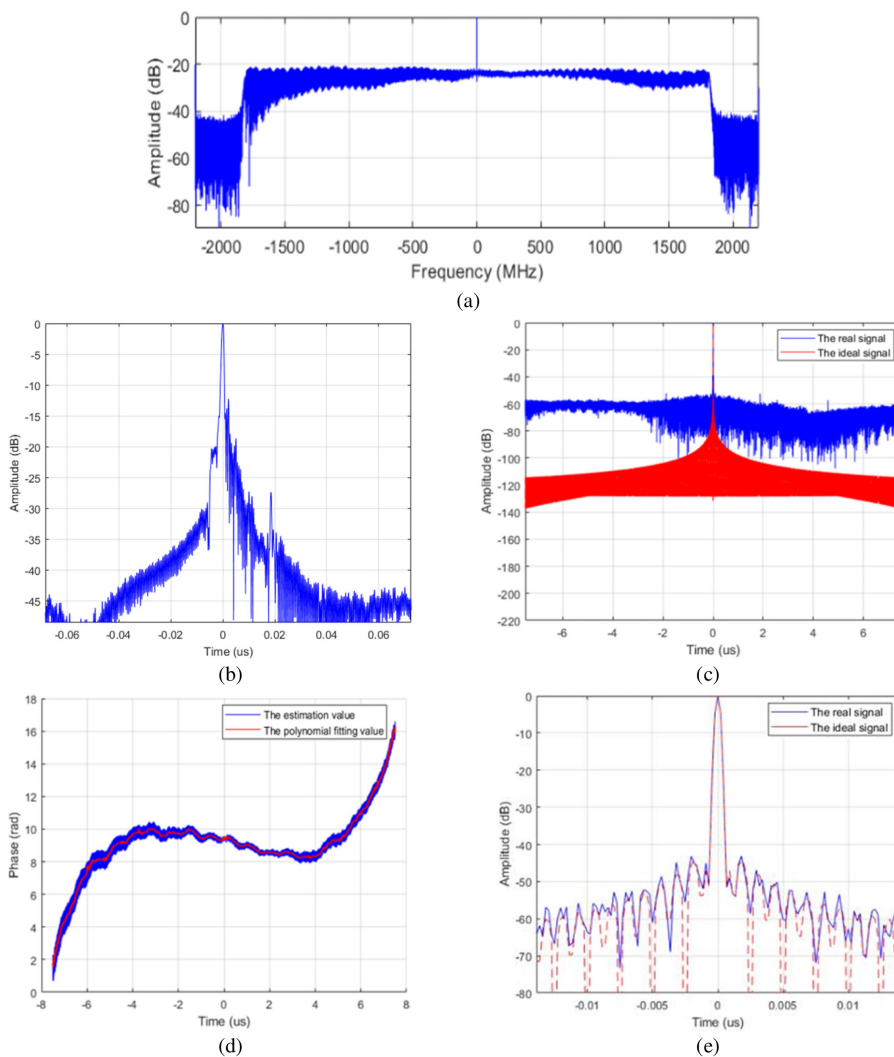


Fig. 13. Processing results of the full-bandwidth 3.6-GHz LFM signal. (a) Spectral. (b) Local zooming part before predistortion calibration. (c) Compression results of ideal and real LFM signals. (d) Phase error. (e) Local zooming part after predistortion calibration.

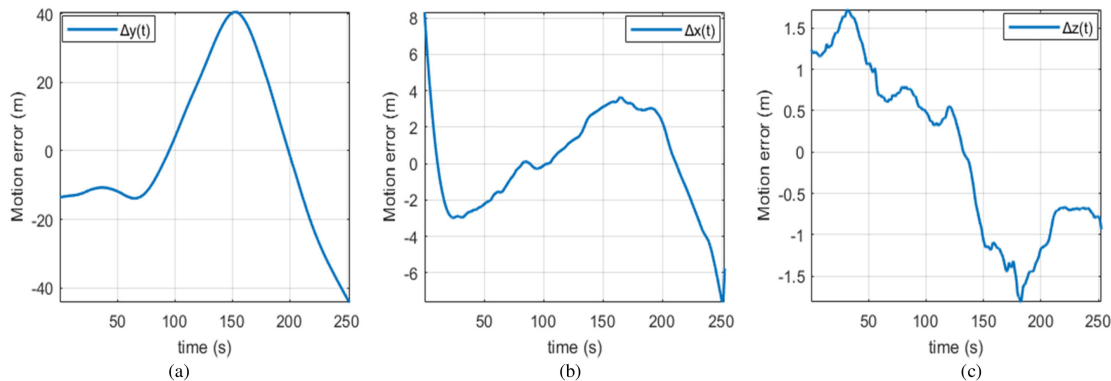


Fig. 14. Motion errors of the 3.6-GHz airborne SAR system after DGPS postprocessing.



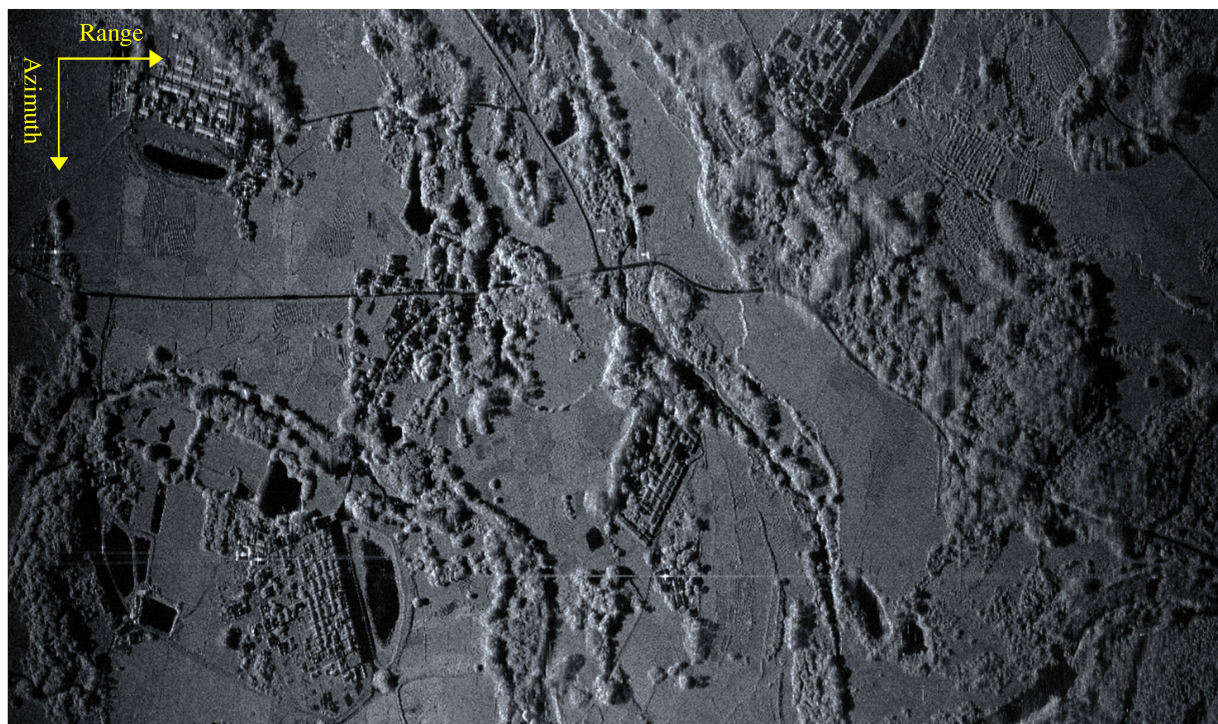


Fig. 15. Global imaging result utilizing the proposed procedure with DGPS-supported.

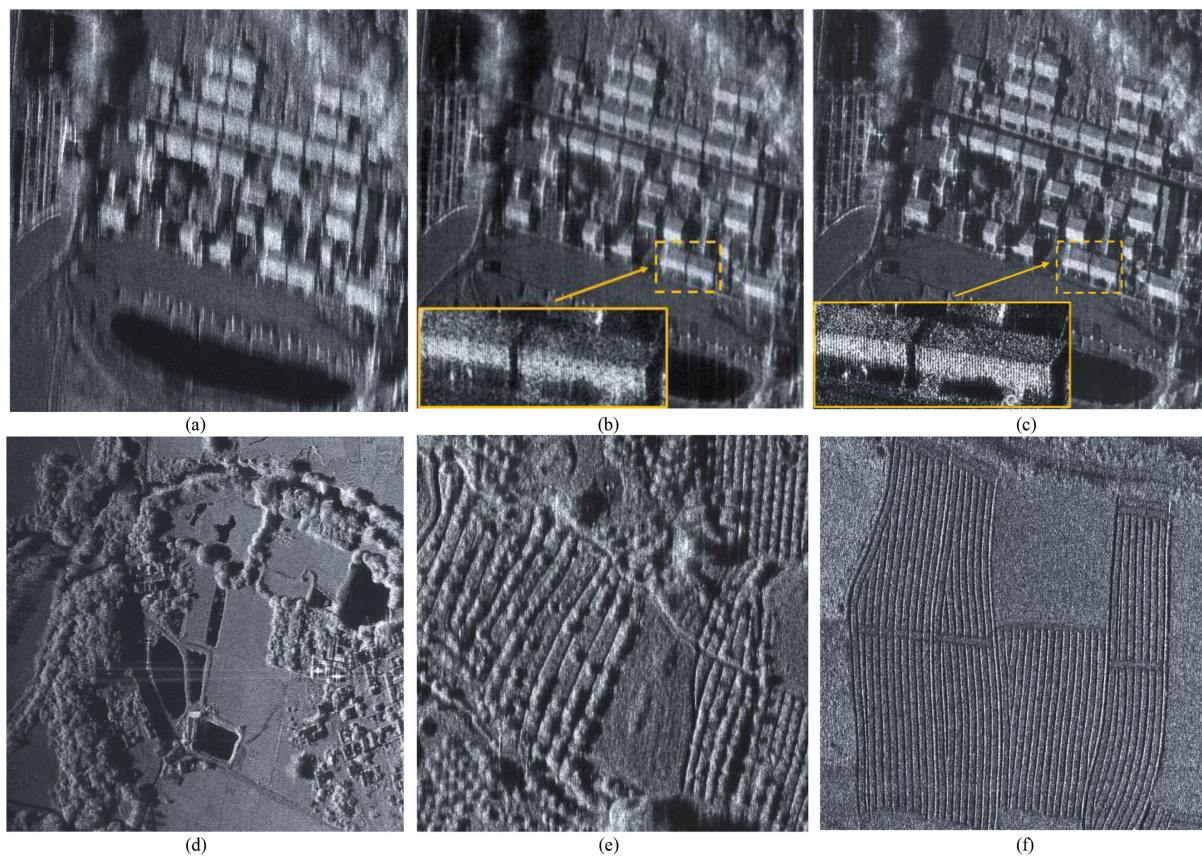


Fig. 16. Local imaging results of full-bandwidth with DGPS-supported. (a) Without MOCO. (b) After MOCO with only IMU device. (c) After MOCO utilizing the proposed procedure with DGPS-supported. (d) Pond scene. (e) Bush scene. (f) Ridge scene.





Fig. 17. Comparison imaging results. (a) Optical scene. (b) Full-bandwidth SAR image.

above, the simulation results are shown in Fig. 12 by utilizing the proposed processing procedure.

As shown in Fig. 12, the proposed processing procedure can compensate the target to the ideal state by separating from the imaging algorithm before RCMC. Meanwhile, it is without the limitation of the imaging algorithm. Therefore, this processing procedure is suitable for the motion error compensation of our experimental 3.6-GHz ultra-high-resolution SAR system.

## VII. EXPERIMENTAL RESULTS

In this section, in order to validate the operability of this airborne system and the effectiveness of the proposed procedure with DGPS-supported, a wireless closed-loop calibration experiment in microwave chamber and an outfield flight experiment were successfully carried out to demonstrate the quality of SAR images in March 2019. Considering that the large bandwidth will aggravate the effect of the inevitable amplitude and phase error in transmitter and further deteriorate the performance of LFM signal, the predistortion signal is constructed by utilizing the link of wireless closed-loop (i.e., a horn antenna unit connecting with the optical delay line locates at decade meters from the transmitting antenna) and is further fed into the radar system to compensate the system errors. The predistortion processing results are shown in Fig. 13.

In the outfield flight experiment, the illuminated scene shows a wide country region of Yangjiang City, which is located near the southeast coastal region of Guangdong province. During the flight, an additional and accurately known position of ground-mounted GPS base station and the airborne-mounted GPS facility conduct GPS observation within 30 km at the same time. Therefore, after the high precise DGPS postprocessing, the outputs of IMU system are shown in Fig 14 in real time. The corresponding 3.6 GHz full-bandwidth imaging results after the proposed MOCO procedure, including different scenarios, are shown in Figs. 15–17, respectively.

Fig. 15 exhibits the global imaging result utilizing the proposed procedure with DGPS-supported and the swath width in range is about 1.25 km. Fig. 16 shows the local zoom imaging results of different scenes and the corresponding comparison, including MOCO only with IMU device and with DGPS-supported. From the comparison of Fig. 16(b) and (c), it is obvious that the rows of tiles edges on a roof can be distinguished with DGPS-supported after the proposed MOCO procedure. Fig. 17 shows the comparison of optical scene and full-bandwidth SAR image. In order to implement the detailed numerical analysis, the local zooming and the profile of the strong scatter point target are shown in Fig. 18. It is clear that the image quality becomes unacceptable without MOCO operation. After MOCO utilizing the proposed procedure with

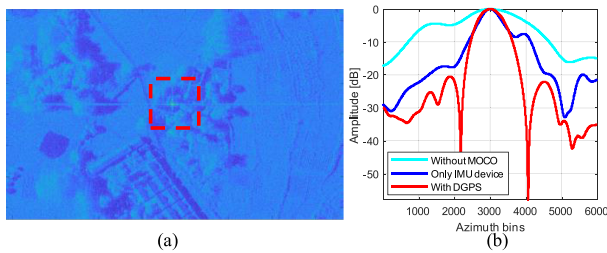


Fig. 18. Comparison results of the profile. (a) Strong scatter point shown in Fig. 15. (b) Profiles of the strong point target with different MOCO strategies.

TABLE III  
NUMERICAL ANALYSIS OF POINT TARGET IN AZIMUTH

Method	IRW	PSLR	ISLR
Without MOCO	4.9303	-2.3791	-6.0458
IMU device	1.7744	-7.5077	-7.7633
DGPS-supported	1.2138	-20.4650	-19.2343

DGPS-supported, the focusing quality is improved greatly. The comparison results are presented Fig. 18(b). During the real data processing, a Kaiser window (i.e.,  $\beta = 2.5$ ) was added. Therefore, the corresponding numerical analysis results of strong target are shown in Table III. The processing results validate the operability of airborne system and the effectiveness of the proposed procedure with DGPS-supported.

### VIII. CONCLUSION

In this article, an outfield experiment of a 3.6-GHz full-bandwidth airborne experimental SAR system operating at X-band, featured by the full-bandwidth transmitting and receiving, has been introduced as a test bed for the development and implementation of the future spaceborne realizations. However, for the ultra-high-resolution SAR system, the improvement of the spatial resolution will aggravate the effect of motion errors. Therefore, a detailed analysis of the effect on motion errors has been given, and an accurate MOCO strategy is presented. In this experiment, considering high accuracy and dependability, the DGPS technology has been applied to adjust the output of the IMU system, which contributes to the high-accuracy MOCO compensation strategy. Finally, the corresponding processing results of an outfield experiment conducted in March 2019 validate the operability of this 3.6-GHz full-bandwidth airborne SAR system and the effectiveness of the proposed procedure with DGPS-supported.

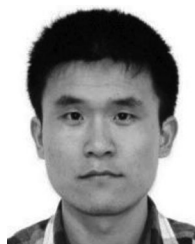
### REFERENCES

- [1] G. Krieger, M. Younis, F. Bordoni, A. Patyuchenko, and A. Moreira, "Advanced concepts for ultra-wide-swath SAR imaging," in *Proc. 7th Eur. Conf. Synth. Aperture Radar*, Friedrichshafen, Germany, 2008, pp. 1–4.
- [2] A. Moreira *et al.*, "Tandem-L: A highly innovative bistatic SAR mission for global observation of dynamic processes on the earth's surface," *IEEE Geosci. Remote Sens. Mag.*, vol. 3, no. 2, pp. 8–23, Jun. 2015.
- [3] I. Sikaneta, C. H. Gierull, and D. Cerutti-Maori, "Optimum signal processing for multichannel SAR: With application to high-resolution wide-swath imaging," *IEEE Trans. Geosci. Remote Sens.*, vol. 52, no. 10, pp. 6095–6109, Oct. 2014.

- [4] N. Gebert, G. Krieger, and A. Moreira, "Digital beamforming on receive: Techniques and optimization strategies for high-resolution and wide-swath SAR imaging," *IEEE Trans. Aerosp. Electron. Syst.*, vol. 45, no. 2, pp. 564–592, Apr. 2009.
- [5] G. Krieger *et al.*, "TanDEM-X: A satellite formation for high-resolution SAR interferometry," *IEEE Trans. Geosci. Remote Sens.*, vol. 45, no. 11, pp. 3317–3341, Nov. 2007.
- [6] N. Gebert, G. Krieger, and A. Moreira, "High resolution wide swath SAR imaging with digital beamforming—Performance analysis, optimization, system design," in *Proc. Eur. Conf. Synthetic Aperture Radar*, Dresden, Germany, Jul. 2006, pp. 341–344.
- [7] C. J. Oliver and S. Quegan, *Understanding Synthetic Aperture Images*. Norwood, MA, USA: Artech House, 1998.
- [8] Y. Huang, Z. Ma and S. Mao, "Stepped-frequency SAR system design and signal processing," in *Proc. Eur. Conf. Synthetic Aperture Radar*, Kiinigswinter, Germany, Mar. 1996, pp. 565–568.
- [9] R.T. Lord and h.L.R. Inggs, "High resolution SAR processing using stepped-frequencies," in *Proc. IEEE Geosci. Remote Sens. Symp.*, Singapore, Aug. 1997, vol. 1, pp. 490–492.
- [10] A. J. Wilkinson, R. T. Lord, and M. R. Inggs, "Stepped-frequency processing by reconstruction of target reflectivity spectrum," in *Proc. South Afr. Symp. Commun. Signal Process.*, 1998, pp. 101–104.
- [11] A. J. Wilkinson, R. T. Lord, and M. R. Inggs, "Stepped-frequency processing by reconstruction of target reflectivity spectrum," in *Proc. South Afr. Symp. Commun. Signal Process.*, Rondebosch, South Africa, 1998, pp. 101–104.
- [12] A. Reigber *et al.*, "Very-high-resolution airborne synthetic aperture radar imaging: Signal processing and applications," *Proc. IEEE*, vol. 101, no. 3, pp. 759–783, Mar. 2013.
- [13] W. Nel, J. Tait, R. Lord, and A. Wilkinson, "The use of a frequency domain stepped frequency technique to obtain high range resolution on the CSIR X-band SAR system," in *Proc. IEEE 6th Afr. Conf. Afr.*, George, South Africa, 2002, vol. 1, pp. 327–332.
- [14] J. H. G. Ender and A. R. Brenner, "PAMIR—A wideband phased array SAR/MTI system," *IEE Proc. - Radar, Sonar Navig.*, vol. 150, no. 3, pp. 165–172, Jun. 2003.
- [15] A. R. Brenner, "Improved radar imaging by centimetre resolution capabilities of the airborne SAR sensor PAMIR," in *Proc. IEEE 14th Int. Radar Symp.*, Dresden, Germany, Jun. 2013, pp. 218–223.
- [16] R. Baqué *et al.*, "SETHI/RAMESSES-NG new performances of the flexible multi-spectral airborne remote sensing research platform," in *Proc. Int. Conf. Radar Syst.*, 2017, pp. 1–4.
- [17] G. Fornaro, G. Franceschetti, and S. Perna, "Motion compensation errors: Effects on the accuracy of airborne SAR images," *IEEE Trans. Aerosp. Electron. Syst.*, vol. 41, no. 4, pp. 1338–1352, Oct. 2005.
- [18] H. M. J. Cantalloube and C. E. Nahum, "Airborne SAR-efficient signal processing for very high resolution," *Proc. IEEE*, vol. 101, no. 3, pp. 784–797, Mar. 2013.
- [19] N. Li, R. Wang, Y. Deng, W. Yu, Z. Zhang, and Y. Liu, "Autofocus correction of residual RCM for VHR SAR sensors with light-small aircraft," *IEEE Trans. Geosci. Remote Sens.*, vol. 55, no. 1, pp. 441–452, Jan. 2017.
- [20] A. Moreira, P. Prats-Iraola, M. Younis, G. Krieger, I. Hajnsek, and K. P. Papathanassiou, "A tutorial on synthetic aperture radar," *IEEE Geosci. Remote Sens. Mag.*, vol. 1, no. 1, pp. 6–43, Mar. 2013.
- [21] M. R. Mosavi and H. Nabavi, "Improving DGPS accuracy using neural network modeling," *Aust. J. Basic Appl. Sci.*, vol. 5, no. 5, pp. 848–856, 2011.
- [22] S. Ahmed, Q. Sultana, and K. D. Rao, "Comparative analysis of DGPS predicted corrections using dynamic neural networks," in *Proc. IEEE Int. Conf. Veh. Electron. Saf.*, Hyderabad, India, 2014, pp. 61–65.
- [23] J. Farrell, M. Grewal, M. Djodot, and M. Barth, "Differential GPS with latency compensation for autonomous navigation," in *Proc. IEEE Int. Symp. Intell. Control*, Dearborn, MI, USA, 1996, pp. 20–24, doi: 10.1109/ISIC.1996.556171.
- [24] L. Zhang, Z. Qiao, M. Xing, L. Yang, and Z. Bao, "A robust motion compensation approach for UAV SAR imagery," *IEEE Trans. Geosci. Remote Sens.*, vol. 50, no. 8, pp. 3202–3218, Aug. 2012.
- [25] J. C. Kirk, "Motion compensation for synthetic aperture radar," *IEEE Trans. Aerosp. Electron. Syst.*, vol. AES-11, no. 3, pp. 338–348, May 1975.
- [26] G. Fornaro, "Trajectory deviations in airborne SAR: Analysis and compensation," *IEEE Trans. Aerosp. Electron. Syst.*, vol. 35, no. 3, pp. 997–1009, Jul. 1999.
- [27] A. Moreira and H. Yonghong, "Airborne SAR processing of highly squinted data using a chirp scaling approach with integrated motion compensation," *IEEE Trans. Geosci. Remote Sens.*, vol. 32, no. 5, pp. 1029–1040, Sep. 1994.



- [28] M. Yang and D. Zhu, "Efficient space-variant motion compensation approach for ultra-high-resolution SAR based on subswath processing," *IEEE J. Sel. Topics Appl. Earth Observ. Remote Sens.*, vol. 11, no. 6, pp. 2090–2103, Jun. 2018.
- [29] X. Zheng, W. Yu, and Z. Li, "A novel algorithm for wide beam SAR motion compensation based on frequency division," in *Proc. IEEE Int. Symp. Geosci. Remote Sens.*, Denver, CO, USA, 2006, pp. 3160–3163.
- [30] D. Blacknell *et al.*, "Geometric accuracy in airborne SAR images," *IEEE Trans. Aerosp. Electron. Syst.*, vol. 25, no. 2, pp. 241–258, Mar. 1989.



**Qingchao Zhao** received the B.S. degree in electronics engineering from the National University of Defense Technology, Changsha, China, in 2010, and the M.S. degree in electronics and communication engineering from the University of Chinese Academy of Sciences, Beijing, China, in 2017. He is currently working toward the Ph.D. degree in communication and information system with the Department of Space Microwave Remote Sensing System, Institute of Electronics, Chinese Academy of Sciences, Beijing, China.

He is currently with the University of Chinese Academy of Sciences. His research interests include high-resolution wide-swath synthetic-aperture radar system design and signal processing.



**Yashi Zhou** was born in Nanchang, China, in 1993. He received the B.S. degree in electronic information science and technology from Central South University, Changsha, China, in 2016. He is currently working toward the Ph.D. degree in communication and information system with the Department of Space Microwave Remote Sensing System, Institute of Electronic, Chinese Academy of Science, Beijing, China.

He is currently with the University of Chinese Academy of Science, Beijing, China. His research interest includes high-resolution wide-swath synthetic-aperture radar signal processing.



**Wei Wang** received the B.S. degree in electronics engineering from the National University of Defence Technology, Changsha, China, in 2008, and the Ph.D. degree in communication and information system from the University of Chinese Academy of Sciences, Beijing, China, in 2016.

In 2016, he joined the Institute of Electronics, Chinese Academy of Sciences, Beijing, China, where he was involved in radar system design and signal processing. His research interests include spaceborne synthetic-aperture radar (SAR) system design and signal processing, high-resolution SAR imaging, multichannel, and DBF SAR.



**Pei Wang** received the B.S. degree in electronics engineering from Xidian University, Xi'an, China, in 2000, the M.S. degree in communication and information system from the Graduate University of Chinese Academy of Sciences, Beijing, China, in 2005, and the Dr. Eng. degree from the University of Chinese Academy of Sciences, Beijing in 2018.

In 2000, he joined the Institute of Electronics, Chinese Academy of Sciences, Beijing, China, where he was an Associate Research Fellow with the Department of Space Microwave Remote Sensing System.

He is currently the Chief Designer or a Main Participator of several national high-resolution spaceborne/airborne imaging radar projects.



**Lei Zhang** was born in Jilin, China, in 1985. He received the Ph.D. degree in communication and information system from the Institute of Electronics, Chinese Academy of Sciences, Beijing, China, in 2014.

He is currently an Associate Research Fellow with the Aerospace Information Research Institute, Chinese Academy of Sciences. His research interests include high-resolution synthetic-aperture radar imaging and signal processing.



**Zhen Chen** received the B.S. degree in electronic information science and technology from Central South University, Changsha, China, in 2017. He is currently working toward the Ph.D. degree in communication and information system with the Department of Space Microwave Remote Sensing System, Institute of Electronic, Chinese Academy of Science, Beijing, China.

He is currently with the University of Chinese Academy of Science, Beijing, China. His research interests include high-resolution wide-swath synthetic-aperture radar signal processing and the motion compensation techniques.

synthetic-aperture radar signal processing and the motion compensation techniques.



**Weidong Yu** (Member, IEEE) was born in Henan, China, in 1969. He received the M.Sc. and the Ph.D. degrees in electrical engineering from the Nanjing University of Aeronautics and Astronautics, Nanjing, China, in 1994 and 1997, respectively.

Since 1997, he has been with the Institute of Electronics, Chinese Academy of Sciences, Beijing, China, where he became a Professor of communication and information systems, in 2000. He has been the Chief Designer for several synthetic-aperture radar (SAR) systems. He is currently the Director of Space Microwave Remote Sensing System Department, Aerospace Information Research Institute, Chinese Academy of Sciences. His research interests include spaceborne and airborne SAR system design and their signal processing.





**Yunkai Deng** (Member, IEEE) received the M.S. degree in electrical engineering from the Beijing Institute of Technology, Beijing, China, in 1993.

In 1993, he joined the Institute of Electronics, Chinese Academy of Sciences (IECAS), Beijing, China, where he was involved in antenna design, microwave circuit design, and spaceborne/airborne synthetic-aperture radar (SAR) technology. Since 1993, he has been a Research Fellow with the Department of Space Microwave Remote Sensing System, IECAS. He has been the Leader of several spaceborne/airborne SAR

programs and developed some key technologies of spaceborne/airborne SAR. Since 2012, he has been a Principal Investigator with the Helmholtz-Chinese Academy of Sciences (CAS) Joint Research Group, Beijing, China, concerning spaceborne microwave remote sensing for prevention and forensic analysis of natural hazards and extreme events. He is currently a Research Scientist with the University of Chinese Academy of Sciences. He has authored or coauthored more than 100 articles since 2002, of which more than 100 are peer-reviewed and well-known journal articles. His research interests include spaceborne/airborne SAR technology for advanced modes, multifunctional radar imaging, and microwave circuit design.

Mr. Deng is a member of the Scientific Board. He was the recipient of several prizes, including the First and Second Class Rewards of National Defense Science and Technology Progress, in 2007; the First Class Reward of the National Scientific and Technological Progress, in 2008; the achievements of the Outstanding Award of the CAS, in 2009; and the First Class Reward of Army Science and Technology Innovation, in 2016, for his outstanding contribution in the SAR field.



**Robert Wang** (Senior Member, IEEE) received the B.S. degree in control engineering from Henan University, Kaifeng, China, in 2002, and the Dr. Eng. degree from the Graduate University of Chinese Academy of Sciences, Beijing, China, in 2007.

In 2007, he joined the Center for Sensor Systems (ZESS), University of Siegen, Siegen, Germany. He was involved in various joint projects supported by ZESS and Fraunhofer-FHR, Wachtberg, Germany, for e.g., the TerraSAR-X/phased array multifunctional imaging radar (PAMIR) hybrid bistatic syn-

thetic aperture radar (SAR) experiment, the PAMIR/stationary bistatic SAR experiment with nonsynchronized oscillator, and the millimeter-wave FMCW SAR data processing. Since 2011, he has been a Research Fellow with the Spaceborne Microwave Remote Sensing System Department, Institute of Electronics, Chinese Academy of Sciences, Beijing, China, where he has been funded by the Hundred Talents Program, Chinese Academy of Sciences. Since 2012, he has been a Co-Principal Investigator (PI) with the Helmholtz-CAS Joint Research Group, Beijing, China, concerning spaceborne microwave remote sensing for prevention and forensic analysis of natural hazards and extreme events. He is also responsible for several national high-resolution spaceborne imaging radar missions supported by the National High-Resolution Earth Observation Major Special Program. He is also the PI of two advanced L-band spaceborne SAR systems that are aimed at global dynamic Earth monitoring. He has authored or coauthored more than 100 peer-reviewed journal articles in SAR imaging technology and *Bistatic SAR System and Signal Processing Technology* (Springer). His research interests include monostatic and multistatic SAR imaging and high-resolution wide-swath spaceborne SAR system and imaging model.

Dr. Wang was the recipient of the National Ten Thousand Talent Program-Young Top-Notch Talent Program, in 2014 and the National Natural Science Funds of China for Excellent Young Scholar, in 2014. He was also the recipient of the Zhao Jiuzhang Award for Outstanding Young Science, in 2015, the First Prize for Military Scientific and Technological Progress, in 2016, the Scientific and Technological Innovation Leading Talent by National High-Level Talents Special Support Plan, in 2017, and the Distinguished Young Scholars from the National Natural Science Foundation of China, in 2018. He was the Session Chair at the European Conference on Synthetic Aperture Radar and the International Geoscience and Remote Sensing Symposium (IGARSS) from 2012 to 2016. He has contributed to invited sessions at the EUSAR from 2008 to 2016, the European Radar Conference in 2009, and IGARSS from 2012 to 2016.